Epitaxial Monolayer MoS$_2$ on Mica with Novel Photoluminescence

Qingqing Ji,[†] Yanfeng Zhang,*[,†,‡] Teng Gao,[†] Yu Zhang,[†,‡] Donglin Ma,[†] Mengxi Liu,[†] Yubin Chen,[†] Xiaofen Qiao,[§] Ping-Heng Tan,[§] Min Kan,[‡] Ji Feng,[∥] Qiang Sun,[‡,⊥] and Zhongfan Liu*[,†]

[†]Center for Nanochemistry (CNC), Beijing National Laboratory for Molecular Sciences, College of Chemistry and Molecular Engineering, Academy for Advanced Interdisciplinary Studies, Peking University, Beijing 100871, People's Republic of China

[‡]Department of Materials Science and Engineering, College of Engineering, Peking University, Beijing 100871, People's Republic of China

[§]State Key Laboratory of Superlattices and Microstructures, Institute of Semiconductors, Chinese Academy of Sciences, Beijing 100083, People's Republic of China

[∥]International Center for Quantum Materials, School of Physics, Peking University, Beijing 100871, People's Republic of China

[⊥]Center for Applied Physics and Technology, Peking University, Beijing 100871, People's Republic of China

S *Supporting Information*

ABSTRACT: Molybdenum disulfide (MoS$_2$) is back in the spotlight because of the indirect-to-direct bandgap tunability and valley related physics emerging in the monolayer regime. However, rigorous control of the monolayer thickness is still a huge challenge for commonly utilized physical exfoliation and chemical synthesis methods. Herein, we have successfully grown predominantly monolayer MoS$_2$ on an inert and nearly lattice-matching mica substrate by using a low-pressure chemical vapor deposition method. The growth is proposed to be mediated by an epitaxial mechanism, and the epitaxial monolayer MoS$_2$ is intrinsically strained on mica due to a small adlayer-substrate lattice mismatch (~2.7%). Photoluminescence (PL) measurements indicate strong single-exciton emission in as-grown MoS$_2$ and room-temperature PL helicity (circular polarization ~0.35) on transferred samples, providing straightforward proof of the high quality of the prepared monolayer crystals. The homogeneously strained high-quality monolayer MoS$_2$ prepared in this study could competitively be exploited for a variety of future applications.

KEYWORDS: Molybdenum disulfide, chemical vapor deposition, van der Waals epitaxy, photoluminescence, valley polarization
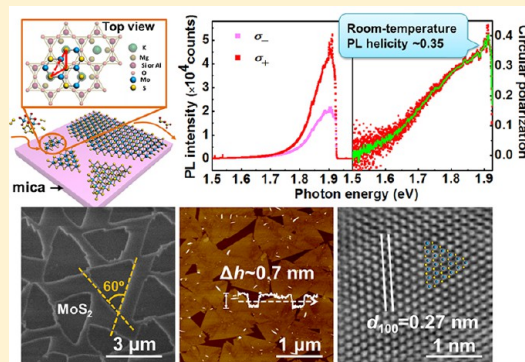
Monolayer molybdenum disulfide (MoS$_2$), a two-dimensional (2D) hexagonal lattice composed of S−Mo−S triple layers, has manifested a wealth of intriguing properties and spurred intense scientific interests. When bulk MoS$_2$ is thinned to the monolayer regime, an indirect-to-direct bandgap transition occurs.[1−4] This contributes to a strong photoluminescence (PL) with sensitive photoresponse.[5−7] Moreover, the absence of centrosymmetry makes monolayer MoS$_2$ valley-selectively excited by circularly polarized light, reflected with remarkable PL helicity.[8−10] This facilitates a new conception of valleytronics[11] with the valley indexes serving as information carriers.

Furthermore, monolayer MoS$_2$ is an ultrastrength material[12] whose energy gap can be easily tuned via strain engineering.[13,14] In addition, the greatly enhanced Coulomb interactions in the direct-gap monolayer MoS$_2$ also make it a perfect model for exploring some fundamental issues of many-body correlated quasiparticles, such as tightly bound trions[15] in condensed matter physics. These unique functionalities make monolayer MoS$_2$ ideally suitable for applications, such as effective photocatalysts,[13] solar energy funnels[14] and excitonic integrated circuits.[16]

However, these versatile applications demand large-scale development of monolayer MoS$_2$ with the above-mentioned properties. Conventionally, monolayer MoS$_2$ is obtained via top-down exfoliation methods,[1,2,6−10,15,17−20] which results in microscale flakes with a random distribution of film thickness. Recently, several bottom-up methods, such as transition metal sulfurization,[21,22] molybdenum oxide sulfurization,[23−25] and decomposition of thiomolybdates,[5,26,27] have been exploited to synthesize MoS$_2$ on SiO$_2$ and other insulating substrates. Nevertheless, the resulting films demonstrated a thickness ranging from monolayer to several layers. Hence, it is of critical need to develop reliable strategies to synthesize macroscopically uniform monolayer MoS$_2$ that could be easily scaled up for batch production.
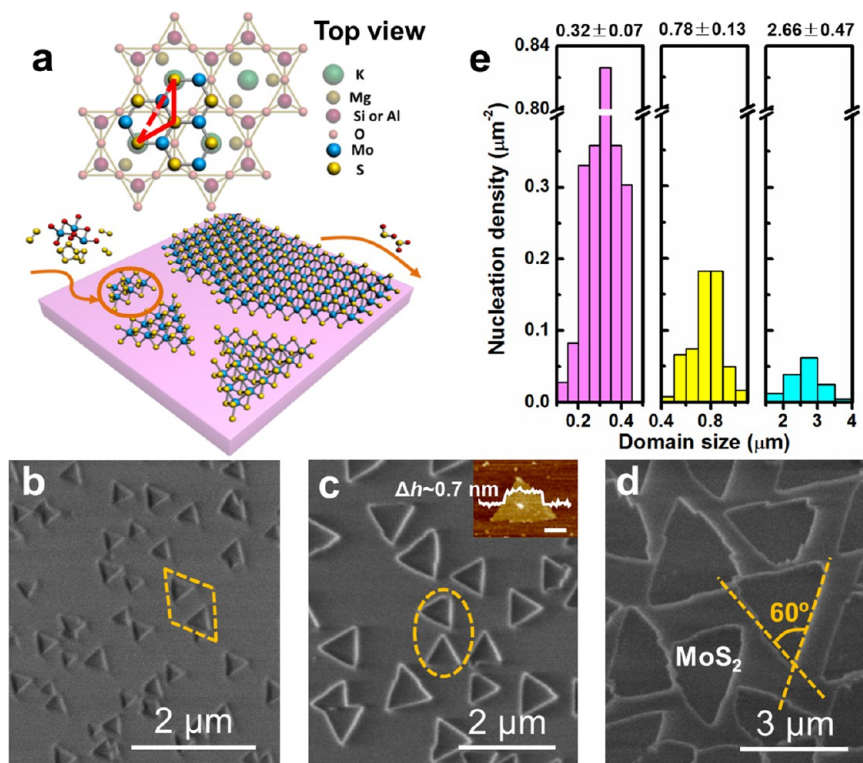
Figure 1. LPCVD synthesis of MoS$_2$ nano/microstructures on mica. (a) A schematic view illustrating the surface reaction during epitaxial growth of MoS$_2$. The upper panel gives probable occupation of MoS$_2$ on mica. (b−d) SEM images showing the initial growth of MoS$_2$ on mica. Inset in (c) is the AFM profile of the MoS$_2$ flake (scale bar 200 nm). (e) Statistical relation of surface nucleation density with flake size obtained from samples shown in b−d (left to right correspondingly, statistics based on SEM images including at least 60 flakes); numbers above the graphs are the averaged flake sizes.

Fluorophlogopite mica (KMg$_3$AlSi$_3$O$_{10}$F$_2$) is considered to be a good van der Waals (vdW) epitaxy substrate for growing 2D materials, because of its atomic flatness, surface inertness, together with the hexagonally arranged in-plane lattice characteristics. These features enable mica suitable for epitaxial growth of materials possessing the same symmetry, such as topological insulators.[28] In particular, the lattice symmetry of fluorophlogopite mica coincident with that of MoS$_2$ could be exploited for the epitaxial growth of monolayer MoS$_2$ on mica.

Herein, we have exploited vdW epitaxy to controllably synthesize centimeter-scale uniform monolayer MoS$_2$ on mica through a low-pressure chemical vapor deposition (LPCVD) process. Moreover, for the first time, we have unraveled the novel PL properties of this intrinsically strained monolayer MoS$_2$, such as intense single excitonic emission on mica, and room-temperature PL helicity variation before and after transfer.

Figure 1a schematically illustrates the surface reaction during the epitaxial MoS$_2$ growth on mica substrates. Details on the growth methodology and experimental setup are provided in Supporting Information Section 1. In the typical process, MoO$_3$ was partially reduced by sulfur vapor to form volatile MoO$_{3-x}$ species,[29] and subsequently they were conveyed downstream by Ar carrier gas, adsorbed on mica, diffusing on the surface, and reacting with sulfur to rearrange into MoS$_2$ layers.

$$S_2 + MoO_{3-x} \rightarrow MoS_2 + SO_2 \tag{1}$$

The upper half of Figure 1a shows the top view of atomic arrangement in mica and the probable occupation sites of MoS$_2$. It is noteworthy that there is a considerable lattice mismatch in the in-plane periodicities of overlayer and

substrate: a(mica) = 0.531 nm, while a(MoS$_2$) = 0.315 nm. However, a(mica) approximates $\sqrt{3}a$(MoS$_2$) (0.546 nm) with a mismatch of −2.7% (negative sign means MoS$_2$ lattice is compressed), smaller than that of Cu(111) to graphene (∼3.9%). This indicates that the rotation of MoS$_2$ lattice by 30° would result in a commensurate structure with mica, which may induce an epitaxial growth of MoS$_2$ on it.

The initial growth pattern of MoS$_2$ on mica substrates, as analyzed by using scanning electron microscope (SEM), is shown in Figure 1b. The darker-contrast flakes on the surface signify MoS$_2$, and the surrounding regions correspond to the mica substrate. All the nucleated MoS$_2$ flakes were triangular shaped, with same orientation and similar size, as highlighted using the dashed rhombus (Figure 1b). Upon prolonging the growth time, MoS$_2$ enlarged in size (Figure 1c) to form larger triangular flakes. Detailed characterization of the sample using atomic force microscopy (AFM) demonstrates a flake thickness of ∼0.7 nm, which is in conformity with that of monolayer MoS$_2$ reported by previous studies.[23,30,31] Further increase in the size of triangular MoS$_2$ flakes to ∼3 μm (Figure 1d) resulted in less straight edges, due to the formation of parallel kinks. These near triangular flakes are still considered to be single crystals. Based on the experimental results reported in previous studies, the edges of the triangles are empirically identified as sulfur terminated ones, along the zigzag orientation.[32−34]

Statistical calculations of the flake size distribution and the nucleation density were subsequently determined (Figure 1e). All the three histograms exhibited a Gaussian-distribution shape, showing average island sizes of 0.32 ± 0.07, 0.78 ± 0.13,
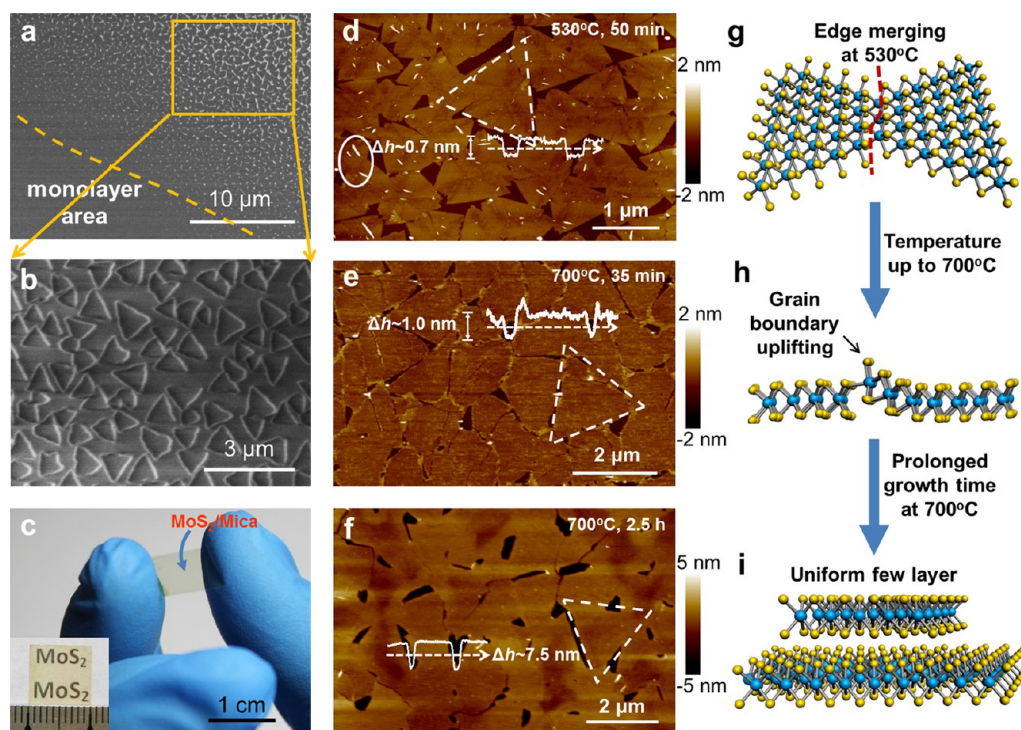
Figure 2. Large-scale layered growth of MoS$_2$ on mica. (a) Growth from submonolayer to monolayer (dashed orange line for eye guide) of MoS$_2$ on a partly sheltered mica substrate. (b) Magnified SEM image of the highlighted part in panel a. (c) Photograph of monolayer MoS$_2$ with full coverage on mica. (d) AFM profile of MoS$_2$ sample with nearly full coverage (~90%), grown at 530 °C for 50 min. The dashed triangle illustrates domain size larger than 1 μm. (e,f) Uniform monolayer and multilayer MoS$_2$ grown at 700 °C for 35 min and 2.5 h, respectively, with similar domain size of ~2 μm. (g,h,i) Atomic models of different growth stages corresponding to panels d, e, and f, respectively.

and 2.66 ± 0.47 μm, corresponding to samples shown in Figure 1b,c,d, respectively. As the flake size increases, the surface nucleation density correspondingly decreases. This implies that the predominant factor controlling the size of MoS$_2$ flakes is the nucleation density, rather than the spreading ability of Mo−S species on mica.

Accordingly, full coverage of monolayer MoS$_2$ on mica could be achieved by increasing the growth time. This was experimentally substantiated by preparing a sample with clear transition from triangular flakes to a complete layer (Figure 2a). The magnified SEM image of the top right part (Figure 2b) shows distinct triangles similar to that of Figure 1c, corresponding to monolayer MoS$_2$ flakes. Meanwhile, the left down part of Figure 2a, with no observable difference in grayness, could reasonably be identified as fully covered monolayer MoS$_2$, exhibiting centimeter-scale uniformity, as depicted by the macroscopic photograph in Figure 2c.

We then obtained the AFM profile of a nearly complete MoS$_2$ layer with coverage of ~90%, which was prepared at 530 °C for 50 min. The height image (Figure 2d) of the triangular domains exhibited nearly homogeneous AFM color contrasts, indicating high thickness uniformity. The line profile of the monolayer MoS$_2$, along the dashed arrow in Figure 2d, gave a monolayer thickness of ~0.7 nm (the corresponding phase image is provided in Supporting Information Figure S2).

Notably, when two MoS$_2$ domains gathered, they preferred to interconnect, rather than overlap with each other, as depicted by the atomic model in Figure 2g. This is a typical characteristic of a 2D growth. Intriguingly, when the full coverage of monolayer was nearly completed, a few zero-dimensional (0D) or quasi-one-dimensional (quasi-1D) structures emerged on the first layer (bright dots or rods of

diameter <5 nm circled in Figure 2d). We believe that these structures could be 0D fullerene-like nanoparticles[35] and 1D nanotubes[36] of MoS$_2$. Upon prolonging the growth time, more particles with larger size were deposited on the first layer (Supporting Information Figure S3). Based on these results, it could be concluded that the MoS$_2$ growth on mica at 530 °C follows an analogous layer-plus-island (or Stranski–Krastanov) growth mode,[37] with the critical layer number of 1. In this case, through a moderate control of the growth kinetics, we can achieve macroscopically uniform MoS$_2$, with the layer thickness strictly limited to monolayer (for more information, see Supporting Information Section 2).

To the best of our knowledge, rigorous control of monolayer thickness with centimeter-scale uniformity has not been reported for MoS$_2$ yet. Our epitaxial CVD method opens up a new avenue to achieve large-scale monolayer MoS$_2$, the size of which is only limited by that of mica substrates. As macroscopic uniformity is essential for device integration and manipulation, the scalably synthesized monolayer MoS$_2$ on mica provides a perfect platform for fabrications of optoelectronic[5−7] and flexible[38] electronic architectures.

In addition, monolayer MoS$_2$ of nearly full coverage was also achieved at 700 °C for 35 min. The AFM profile of the resulting film (Figure 2e) shows a film thickness of ~1 nm and surface roughness of ~0.39 nm, which are both higher than those obtained on samples grown at 530 °C for 50 min (0.7 and 0.27 nm, correspondingly). Figure 2e also evidenced slightly protruded interdomain junctions, which probably arises from the uplifting of grain boundaries (GBs), as depicted in Figure 2h. The higher surface roughness along with the uplifted GBs at 700 °C implies relaxed strain (or lattice matching) restriction of the first epitaxial layer. Further prolonging of
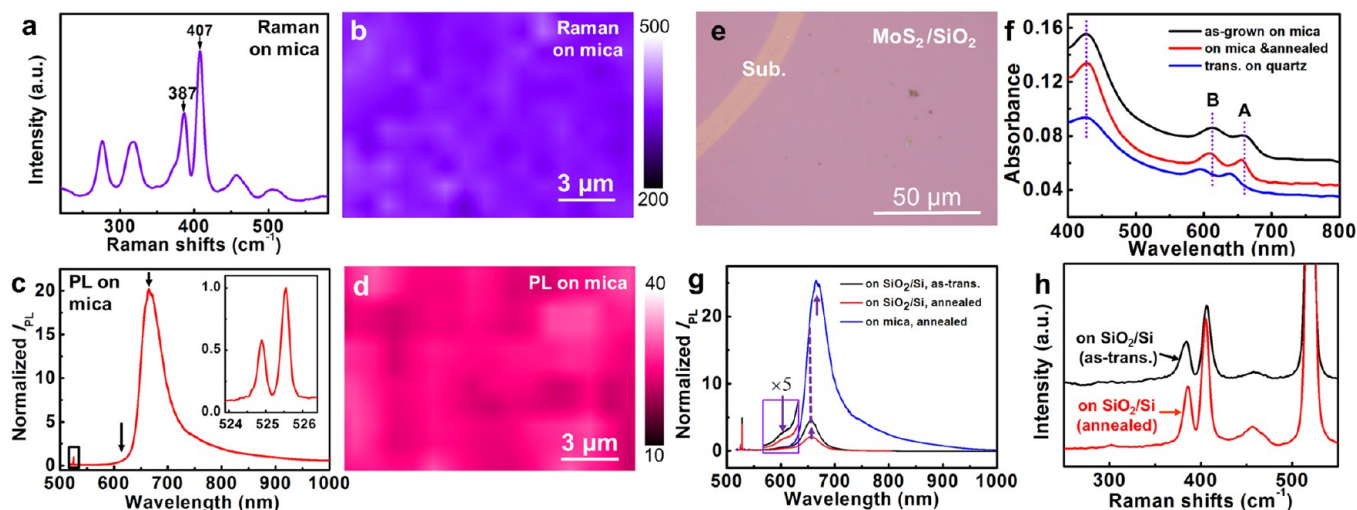
Figure 3. Spectroscopic characterization and transferability of monolayer MoS_2 grown on mica. (a) Raman spectrum of as-grown monolayer MoS_2 on mica. (b) Mapping of Raman characteristic peak intensity integrated from 370 to 420 cm^{-1} within a $15 \times 10 \ \mu m^2$ area. (c) Normalized PL spectrum of annealed monolayer MoS_2/mica. The PL intensity is normalized by Raman A_1' phonon peak at ~525.5 nm (407 cm^{-1} in Raman shifts). The inset is the magnified spectrum showing characteristic Raman peaks. (d) Mapping of normalized PL intensity on the same area of panel c. (e) Optical photograph of monolayer MoS_2 transferred onto SiO_2/Si. (f) UV−vis spectra of monolayer MoS_2 before and after transfer. (g,h) Raman and PL spectra, respectively, of the transferred MoS_2. The PL intensity of B excitonic peak in panel g is 5-fold amplified to be identified clearly, and the two lines in panel h are vertically offset.

growth time to 2.5 h resulted in uniform few-layered MoS_2 with a thickness of ~7.5 nm (Figure 2f,i).

We systematically characterized the monolayer MoS_2 grown at 530 °C. Raman measurements performed on the sample (Figure 3a) exhibited two characteristic peaks, in parallel with two phonon modes: out-of-plane vibration of S atoms (A_1') at ~407 cm^{-1} and in-plane vibration of Mo and S atoms (E') at ~387 cm^{-1}, with a frequency difference Δ ~20 cm^{-1}. According to the "Δ-thickness relation" established by previous works based on exfoliated samples,[10,30,39] the observed frequency difference could be correlated to that of monolayer MoS_2.

Compared to the Raman spectra of exfoliated monolayer MoS_2 on SiO_2/Si (A_1' and E' peaks at ~403 and 384 cm^{-1}, respectively[30]), a phonon mode stiffening, reflected with blueshift of both characteristic peaks by 3−4 cm^{-1}, was ubiquitously observed in all the samples prepared in this study. This phenomenon is expected to be closely related to the compressive strain induced by adlayer-substrate lattice mismatch, as is similarly reported for strained graphene, whose G and 2D peaks contemporarily red-shifted with external tensile force.[40,41] In any case, the phonon stiffening could be considered as an additional evidence of the epitaxial growth. Additionally, we also performed the Raman mapping of MoS_2 characteristic peak intensities (integrated from 370 to 420 cm^{-1}), to understand the thickness uniformity at the micrometer scale (Figure 3b). It could be clearly evidenced that the film is nearly homogeneous even at almost 10-μm scale, except for bits of thicker areas dominating less than 5% of the surface.

Figure 3c shows the typical PL spectrum of monolayer MoS_2 grown on mica obtained by annealing at 1000 °C under sulfur atmosphere. The reason for annealing the sample is explained in Supporting Information Figure S5 and relevant discussions. A strikingly strong PL peak (A excitonic emission) at ~665 nm, with no shoulder peak at ~610 nm (B excitonic emission) was observed (Figure 3c). Such single PL peak has been reported

only in exfoliated monolayer MoS_2 suspended on holed Si substrates[2] to our knowledge. Hence, the observation of single (A excitonic emission) peak is again a strong evidence that the monolayer MoS_2 synthesized here is undoubtedly of high quality. It is worth mentioning that the distinct peak tailing on the longer wavelength side is actually the PL background of mica substrates (see Supporting Information Figure S6).

The PL spectrum was normalized by Raman A_1' peak intensity, to rule out the external effects, such as laser power and local electric field factors.[1] The normalized PL intensity provided direct information on the PL quantum efficiency, which was observed to be significantly thickness dependent.[1,2] In the case of the monolayer MoS_2/mica sample prepared in this study, a strong PL intensity was usually accompanied by a better Raman signal, as shown in Figure 3c. Hence the normalized PL intensity exceeding 20 could be regarded as PL enhancement. In addition, the mapping of A peak intensity (Figure 3d) was homogeneous over the whole region, demonstrating high thickness uniformity.

Moreover, the prepared monolayer MoS_2 sample (coverage >90%) was transferred intactly onto oxidized Si substrates (with 300 nm oxide layer) with a portable transfer method. The optical image of the transferred film (Figure 3e) shows a uniform purple-like contrast corresponding to MoS_2 across hundreds of micrometers, as distinguished from Si substrates with a khaki color. Considering that MoS_2 layers of different thickness may present distinct color contrasts in optical images, the nearly uniform contrast in the MoS_2 regions indicate uniform monolayer thickness.[32,42] To substantiate this conclusion, the intact nature of the transferred sample was also confirmed by using SEM (Supporting Information Figure S7).

Taking advantage of the transparency of mica in visible light region (Supporting Information Figure S4), we further conducted UV−vis absorption characterization of the as-grown monolayer MoS_2 sample (black line in Figure 3e). The resulting UV−vis spectrum exhibited two exciton
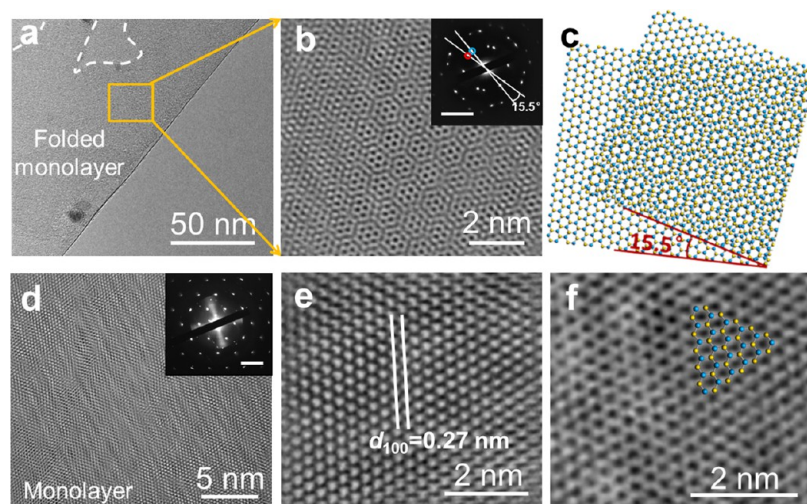
Figure 4. HRTEM characterization of monolayer MoS_2. (a) Folded edge of monolayer MoS_2, with only one dark line contrast aligned at the edge. (b) Zoomed-in image on (a) exhibits a randomly stacked region. Inset of (b) is the corresponding electron diffraction pattern (scale bar 5 nm^{-1}). Two sets of hexagonally arranged spots rotated by 15.5° were circled. (c) Atomic model of the folded edge. (d−f) Monolayer area with two typical images shown in panels e and f. The inset of panel d is the diffraction pattern (scale bar 5 nm^{-1}) for the monolayer area. (Panels d−f are filtered HRTEM images. Original data can be found in Supporting Information Figure S8.)

absorption bands at 657 nm (1.89 eV) and 612 nm (2.03 eV), labeled as A and B, respectively. These bands are believed to originate from the direct bandgap transition at K point, with energy split from valence band spin−orbital coupling.[1,2] The energy difference corresponding to the two peaks was observed to be 0.14 eV, which is in good agreement with the theoretical value of 0.148 eV, calculated for monolayer MoS_2.[43] This perfect agreement evidenced not only the fine electronic structure, but also the high crystal quality of the prepared monolayer MoS_2/mica sample.

Upon annealing the as-grown sample under sulfur atmosphere at 1000 °C, the A and B absorption bands slightly blueshifted by 2 and 4 nm, respectively (red line in Figure 3f). However, when transferred onto quartz substrates (to corroborate PL spectra on SiO_2/Si in Figure 3h), the resulting sample exhibited two absorption bands (A and B) both blueshifted by ∼60 meV (blue line in Figure 3f). This suggests probable band structure alteration during the transfer process.

We further recorded the PL spectra of MoS_2 transferred onto oxidized Si substrates. After transfer, the sample exhibited typical PL features with A and B excitonic emission peaks centered at ∼656 and 605 nm, respectively (Figure 3g). Notably, the PL intensity of monolayer MoS_2 transferred on SiO_2/Si was prominently weaker than that grown on mica. This could probably be due to the enhanced charge trapping from the SiO_2/Si substrate. Meanwhile, A exciton PL peak blueshifted from ∼665 nm to ∼656 nm after transfer (Figure 3g), consistent with the blueshifted absorption bands in the UV−vis spectra for transferred samples (blue line in Figure 3f). The concurrent blueshift observed in PL and absorption spectra after transfer can be regarded as an evidence of the possible lattice strain releasing, considering the direct bandgap tunability of monolayer MoS_2 via strain engineering.[13,14]

For comparison, we also annealed the MoS_2 sample transferred onto SiO_2/Si substrate, at 900 °C under sulfur atmosphere. Figure 3h shows the Raman spectra of the transferred sample before and after annealing. It could be observed that the annealing treatment enhanced the characteristic Raman peaks (Figure 3h). However, on the contrary, the

normalized intensity of A excitonic emission in the corresponding PL spectra (Figure 3g) reduced significantly. These observations imply that the charge impurity density of Si substrates might have been improved further, as a result of annealing.

High-resolution transmission electron microscopic (HRTEM) analysis was performed to explore the monolayer nature as well as the crystal quality of the prepared MoS_2 after transfer. The low magnification HRTEM images (Supporting Information Figures S10 and S11) exhibit a continuous film on the copper grids. Around the occasionally observed broken regions, some obvious folding of the film could be clearly distinguished, based on the contrast with respect to the adjacent regions (Figure 4a). In general, edge folding is a common phenomenon in two-dimensional materials, like graphene, which could be effectively utilized to determine the number of layers.[44] That is to say, the single dark line at the folded edge could be correlated to a monolayer.

The HRTEM image for the folded region exhibited a moiré pattern with periodicity of ∼1.1 nm (Figure 4b), corresponding to interlayer misorientation of ∼16°. This folding induced misorientation was reconfirmed by the selected area electron diffraction (SAED) pattern (inset of Figure 4b) collected over a scale of 200 × 200 nm^2, which consists of two sets of hexagonally arranged diffraction spots rotated by ∼15.5° with each other. The first-order diffraction spots correspond to (100) planes, with which we calculated $d(100)$ equaling 0.27 nm, thus MoS_2 in-plane lattice constant $a(MoS_2)$ was determined to be ∼0.31 nm, which is in agreement with the bulk value of 0.315 nm. For visualization, the atomic model of this folded edge is depicted in Figure 4c.

We further examined the area away from the folded edge. The HRTEM images of this region reveal perfect atomic lattices extending over at least several hundred nanometers, as shown in Figure 4d. The corresponding SAED pattern shown as an inset exhibits only one set of diffraction spots, indicating the single crystalline nature of the film. Further high-resolution images present two kinds of contrasts with triangular or hexagonal shape (Figure 4e,f), which agrees well with the data
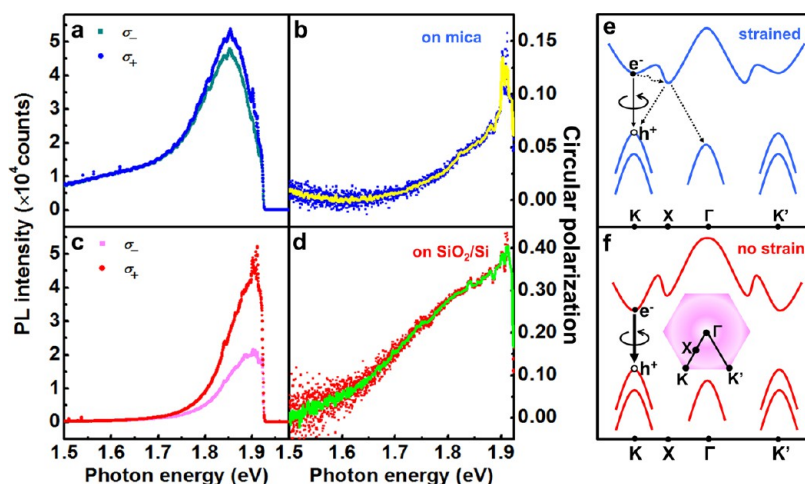
Figure 5. Valley-polarized emission from our monolayer MoS$_2$ before and after transfer. The helicity resolved PL spectra are shown in panels a and c, and the corresponding circular polarization scatter-plotted as function of emissive photon energy are displayed in panels b and d. Panels a and b were measured on monolayer MoS$_2$/mica obtained by annealing at 1000 °C, while c and d were acquired on MoS$_2$ transferred onto SiO$_2$/Si. The complementary colored curves inside b and d are adjacent-point-averaged results of circular polarization. (e) Schematic band structure along K-Γ-K′ direction for the compressively strained monolayer MoS$_2$. Only the direct-gap emission at K valley (solid arrow) shows helicity, and the indirect-gap transitions (marked with dashed arrows) give nonpolarized emissions. (f) Schematic band structure for monolayer MoS$_2$ with zero strain. The first Brillouin Zone of monolayer MoS$_2$ is plotted as an inset.

published on exfoliated MoS$_2$.[45] The TEM results thus signify that the MoS$_2$ prepared in this study is almost defect-free and strictly monolayer.

Furthermore, the high crystal quality of the prepared monolayer MoS$_2$ was certified through its perfect valley related optical properties, considering that the PL helicity could be strongly reduced by intervalley scattering through defects and impurities. For this, helicity resolved PL measurements were performed on MoS$_2$ before and after transfer (Figure 5). The sample kept at room temperature (300 K) was excited with right-handed (σ_+) circularly polarized He−Ne laser at 632.8 nm. The degree of circular polarization can be defined as follows:

$$P(\sigma_+) = \frac{I(\sigma_+) - I(\sigma_-)}{I(\sigma_+) + I(\sigma_-)} \qquad (2)$$

where $I(\sigma_\pm)$ denotes the PL intensity of the right (left)-handed component. Interestingly, as-grown monolayer MoS$_2$ on mica exhibited a low PL helicity of less than 0.1 (Figure 5a,b); whereas after the monolayer MoS$_2$ was transferred onto SiO$_2$/Si, $P(\sigma_+)$ dramatically increased to a maximum of ~0.35 (Figure 5c,d). The observed high value of PL helicity at room temperature indicates a long lifetime for the photogenerated excitons in their original valley at K point (Figure 5f), strongly suggestive of the ultrahigh crystal quality of the CVD MoS$_2$. By contrast, the relatively low PL helicity for as-grown samples is probably due to the band structure modulation of MoS$_2$ by its conformation to the mica substrate. A direct-to-indirect bandgap transition (Supporting Information Figure S12) probably occurs as demonstrated by our density functional theory (DFT) calculations where a small compressive strain of about −1.5% was applied. This would contribute more pathways for exciton relaxation to neighboring valleys (Figure 5e indicated with dashed arrows), and hence the direct-gap recombination within the K valley was suppressed, corresponding to a smaller PL helicity (for details, see Supporting Information Section 7).

In summary, we have successfully synthesized centimeter-scale, strictly monolayer, high-quality MoS$_2$ on the nearly lattice-matching mica substrates, with the growth following an epitaxial mechanism. This synthesis method combines vdW epitaxy with LPCVD, opening up the possibility of achieving batch production of monolayer MoS$_2$ with intrinsic strain in a simple process. The high PL helicity (~0.35) of transferred sample obtained at room temperature evidently demonstrates the ultrahigh quality of the prepared MoS$_2$, enabling it a prototype for exploring valley related physics. That is, we believe the proposed strategy would pave the way for applications of CVD synthesized monolayer MoS$_2$ in future electronics and optoelectronics.

Methods. *Monolayer MoS$_2$ Epitaxial Growth and Transfer.* Large-area monolayer MoS$_2$ were grown inside a multi-temperature-zone tubular furnace (Lindberg/Blue M) equipped with a 1-in.-diameter quartz tube. Sulfur powder was placed outside the hot zone, and was mildly sublimated with heating belts at ~100 °C. MoO$_3$ powder (Alfa Aesar, purity 99.9%) and freshly cleaved fluorophlogopite mica substrates (thickness around 50 μm) were successively placed in the hot center inside the tube furnace. Argon was used as the carrier gas to convey MoO$_{3-x}$ vapor species to the downstream mica substrates. The tube was pumped down to a base pressure of ~1 Pa and flushed with Ar carrier gas repeatedly to guarantee a favorable growth atmosphere. Typical growth conditions were pressure of 30 Pa, carrier gas flow rate of 50 sccm, growth temperature of 530 °C and growth time of 30−60 min. Subsequently, the as-grown MoS$_2$ sample was transferred to arbitrary substrates, such as oxidized silicon wafer, with the aid of poly(methyl methacrylate) by using a portable transfer method. For this, hydrofluoric acid (20 wt %) was used as the etchant to detach MoS$_2$ adlayer from mica.

Characterizations of Epitaxial Monolayer MoS$_2$. The prepared samples were systematically characterized using optical microscopy (Olympus DX51), Raman spectroscopy (Horiba, LabRAM HR-800), UV−vis−IR (Perkin-Elmer Lambda 950 spectrophotometer), AFM (Vecco Nanoscope

IIIa), SEM (Hitachi S-4800; acceleration voltage of 1−5 kV) and TEM (JEOL JEM-2100F LaB6; acceleration voltage, 200 kV). A lacey carbon film supported on copper grids was used for TEM characterization, onto which MoS_2 layer was transferred with the method described in the last paragraph.

Circularly Polarized PL Measurements. Helicity-resolved PL measurements were carried out using a Jobin-Yvon HR800 Raman system with an indigenously developed system for circularly polarized excitation. The excitation light of 633 nm in wavelength, obtained using a HeNe laser, was passed through a Soleil Babinet Compensator to generate a circularly polarized light. The state of circular polarization was confirmed on the sample location. An objective of relatively small numerical aperture (0.55) was used to achieve close-to-normal-incidence excitation with negligible photon spin in the sample in-plane direction. The polarization was set to σ_+, and the PL polarization (σ_+ or σ_-) was analyzed by using a quarter-wave plate placed in front of a fixed Glan-Thomson linear polarizer. The whole setup provided a rejection ratio better than 5% in σ_+ and σ_- configuration, over the spectral range of interest. The excitation power of 50 μW was used to avoid sample heating.

ASSOCIATED CONTENT

S **Supporting Information**

Detailed description and discussion of the epitaxial CVD growth, temperature regulated growth mode, and explanation for the low PL helicity of as-grown monolayer MoS_2 on mica, as well as supplementary figures. This material is available free of charge via the Internet at http://pubs.acs.org.

AUTHOR INFORMATION

Corresponding Author

*E-mail: yanfengzhang@pku.edu.cn (Y.Z.); zfliu@pku.edu.cn (Z.L.).

Notes

The authors declare no competing financial interest.

ACKNOWLEDGMENTS

REFERENCES

(1) Splendiani, A.; Sun, L.; Zhang, Y. B.; Li, T. S.; Kim, J.; Chim, C. Y.; Galli, G.; Wang, F. *Nano Lett.* **2010**, *10* (4), 1271−1275.

(2) Mak, K. F.; Lee, C.; Hone, J.; Shan, J.; Heinz, T. F. *Phys. Rev. Lett.* **2010**, *105* (13), 136805.

(3) Huang, X.; Zeng, Z.; Zhang, H. *Chem. Soc. Rev.* **2013**, *42* (5), 1934−1946.

(4) Chhowalla, M.; Shin, H. S.; Eda, G.; Li, L.-J.; Loh, K. P.; Zhang, H. *Nat. Chem.* **2013**, *5* (4), 263−275.

(5) Tsai, D.-S.; Liu, K.-K.; Lien, D.-H.; Tsai, M.-L.; Kang, C.-F.; Lin, C.-A.; Li, L.-J.; He, J.-H. *ACS Nano* **2013**, *7* (5), 3905−3911.

(6) Yin, Z. Y.; Li, H.; Li, H.; Jiang, L.; Shi, Y. M.; Sun, Y. H.; Lu, G.; Zhang, Q.; Chen, X. D.; Zhang, H. *ACS Nano* **2012**, *6* (1), 74−80.

(7) Choi, W.; Cho, M. Y.; Konar, A.; Lee, J. H.; Cha, G.-B.; Hong, S. C.; Kim, S.; Kim, J.; Jena, D.; Joo, J.; Kim, S. *Adv. Mater.* **2012**, *24* (43), 5832−5836.

(8) Cao, T.; Wang, G.; Han, W.; Ye, H.; Zhu, C.; Shi, J.; Niu, Q.; Tan, P.; Wang, E.; Liu, B.; Feng, J. *Nat. Commun.* **2012**, *3*, 887.

(9) Mak, K. F.; He, K. L.; Shan, J.; Heinz, T. F. *Nat. Nanotechnol.* **2012**, *7* (8), 494−498.

(10) Zeng, H. L.; Dai, J. F.; Yao, W.; Xiao, D.; Cui, X. D. *Nat. Nanotechnol.* **2012**, *7* (8), 490−493.

(11) Xiao, D.; Liu, G. B.; Feng, W. X.; Xu, X. D.; Yao, W. *Phys. Rev. Lett.* **2012**, *108* (19), 196802.

(12) Bertolazzi, S.; Brivio, J.; Kis, A. *ACS Nano* **2011**, *5* (12), 9703−9709.

(13) Li, Y.; Li, Y.; Araujo, C. M.; Luo, W.; Ahuja, R. *arXiv.org, e-Print Arch., Condens. Matter* **2012**, No. arXiv:1211.4052, DOI: 10.1039/C3CY00207A.

(14) Feng, J.; Qian, X.; Huang, C.-W.; Li, J. *Nat. Photon.* **2012**, *6* (12), 866−872.

(15) Mak, K. F.; He, K.; Lee, C.; Lee, G. H.; Hone, J.; Heinz, T. F.; Shan, J. *Nat. Mater.* **2012**, *12* (3), 207−211.

(16) High, A. A.; Novitskaya, E. E.; Butov, L. V.; Hanson, M.; Gossard, A. C. *Science* **2008**, *321* (5886), 229−231.

(17) Eda, G.; Yamaguchi, H.; Voiry, D.; Fujita, T.; Chen, M. W.; Chhowalla, M. *Nano Lett.* **2011**, *11* (12), 5111−5116.

(18) Coleman, J. N.; Lotya, M.; O'Neill, A.; Bergin, S. D.; King, P. J.; Khan, U.; Young, K.; Gaucher, A.; De, S.; Smith, R. J.; Shvets, I. V.; Arora, S. K.; Stanton, G.; Kim, H. Y.; Lee, K.; Kim, G. T.; Duesberg, G. S.; Hallam, T.; Boland, J. J.; Wang, J. J.; Donegan, J. F.; Grunlan, J. C.; Moriarty, G.; Shmeliov, A.; Nicholls, R. J.; Perkins, J. M.; Grieveson, E. M.; Theuwissen, K.; McComb, D. W.; Nellist, P. D.; Nicolosi, V. *Science* **2011**, *331* (6017), 568−571.

(19) Zeng, Z.; Yin, Z.; Huang, X.; Li, H.; He, Q.; Lu, G.; Boey, F.; Zhang, H. *Angew. Chem., Int. Ed.* **2011**, *50* (47), 11093−11097.

(20) Li, H.; Yin, Z.; He, Q.; Li, H.; Huang, X.; Lu, G.; Fam, D. W. H.; Tok, A. I. Y.; Zhang, Q.; Zhang, H. *Small* **2012**, *8* (1), 63−67.

(21) Kim, D.; Sun, D. Z.; Lu, W. H.; Cheng, Z. H.; Zhu, Y. M.; Le, D.; Rahman, T. S.; Bartels, L. *Langmuir* **2011**, *27* (18), 11650−11653.

(22) Zhan, Y. J.; Liu, Z.; Najmaei, S.; Ajayan, P. M.; Lou, J. *Small* **2012**, *8* (7), 966−971.

(23) Lee, Y. H.; Zhang, X. Q.; Zhang, W. J.; Chang, M. T.; Lin, C. T.; Chang, K. D.; Yu, Y. C.; Wang, J. T. W.; Chang, C. S.; Li, L. J.; Lin, T. W. *Adv. Mater.* **2012**, *24* (17), 2320−2325.

(24) Wang, X.; Feng, H.; Wu, Y.; Jiao, L. *J. Am. Chem. Soc.* **2013**, *135* (14), 5304−5307.

(25) Lin, Y. C.; Zhang, W. J.; Huang, J. K.; Liu, K. K.; Lee, Y. H.; Liang, C. T.; Chu, C. W.; Li, L. J. *Nanoscale* **2012**, *4* (20), 6637−6641.

(26) Liu, K. K.; Zhang, W. J.; Lee, Y. H.; Lin, Y. C.; Chang, M. T.; Su, C.; Chang, C. S.; Li, H.; Shi, Y. M.; Zhang, H.; Lai, C. S.; Li, L. J. *Nano Lett.* **2012**, *12* (3), 1538−1544.

(27) Shi, Y. M.; Zhou, W.; Lu, A. Y.; Fang, W. J.; Lee, Y. H.; Hsu, A. L.; Kim, S. M.; Kim, K. K.; Yang, H. Y.; Li, L. J.; Idrobo, J. C.; Kong, J. *Nano Lett.* **2012**, *12* (6), 2784−2791.

(28) Li, H.; Cao, J.; Zheng, W.; Chen, Y.; Wu, D.; Dang, W.; Wang, K.; Peng, H.; Liu, Z. *J. Am. Chem. Soc.* **2012**, *134* (14), 6132−6135.

(29) Feldman, Y.; Wasserman, E.; Srolovitz, D. J.; Tenne, R. *Science* **1995**, *267* (5195), 222−225.

(30) Lee, C.; Yan, H.; Brus, L. E.; Heinz, T. F.; Hone, J.; Ryu, S. *ACS Nano* **2010**, *4* (5), 2695−2700.

(31) Radisavljevic, B.; Radenovic, A.; Brivio, J.; Giacometti, V.; Kis, A. *Nat. Nanotechnol.* **2011**, *6* (3), 147−150.

(32) van der Zande, A. M.; Huang, P. Y.; Chenet, D. A.; Berkelbach, T. C.; You, Y.; Lee, G.-H.; Heinz, T. F.; Reichman, D. R.; Muller, D. A.; Hone, J. C. *arXiv.org, e-Print Arch., Condens. Matter* **2013**, No. arXiv:1301.1985, DOI: 10.1038/nmat3633.

(33) Lauritsen, J. V.; Kibsgaard, J.; Helveg, S.; Topsøe, H.; Clausen, B. S.; Lægsgaard, E.; Besenbacher, F. *Nat. Nanotechnol.* **2007**, *2* (1), 53−58.

(34) Helveg, S.; Lauritsen, J. V.; Lægsgaard, E.; Stensgaard, I.; Nørskov, J. K.; Clausen, B.; Topsøe, H.; Besenbacher, F. *Phys. Rev. Lett.* **2000**, *84* (5), 951−954.

(35) Chhowalla, M.; Amaratunga, G. A. J. *Nature* **2000**, *407* (6801), 164−167.

(36) Remskar, M.; Mrzel, A.; Skraba, Z.; Jesih, A.; Ceh, M.; Demšar, J.; Stadelmann, P.; Lévy, F.; Mihailovic, D. *Science* **2001**, *292* (5516), 479−481.

(37) Bauer, E.; van der Merwe, J. H. *Phys. Rev. B* **1986**, *33* (6), 3657−3671.

(38) Peng, H.; Dang, W.; Cao, J.; Chen, Y.; Wu, D.; Zheng, W.; Li, H.; Shen, Z.-X.; Liu, Z. *Nat. Chem.* **2012**, *4* (4), 281−286.

(39) Zhang, X.; Han, W. P.; Wu, J. B.; Milana, S.; Lu, Y.; Li, Q. Q.; Ferrari, A. C.; Tan, P. H. *Phys. Rev. B* **2013**, *87* (11), 115413.

(40) Ni, Z. H.; Yu, T.; Lu, Y. H.; Wang, Y. Y.; Feng, Y. P.; Shen, Z. X. *ACS Nano* **2008**, *2* (11), 2301−2305.

(41) Huang, M. Y.; Yan, H. G.; Chen, C. Y.; Song, D. H.; Heinz, T. F.; Hone, J. *Proc. Natl. Acad. Sci. U.S.A.* **2009**, *106* (18), 7304−7308.

(42) Najmaei, S.; Liu, Z.; Zhou, W.; Zou, X.; Shi, G.; Lei, S.; Yakobson, B. I.; Idrobo, J. C.; Ajayan, P. M.; Lou, J. *arXiv.org, e-Print Arch., Condens. Matter* **2013**, No. arXiv:1301.2812, DOI: 10.1038/nmat3673.

(43) Zhu, Z. Y.; Cheng, Y. C.; Schwingenschlogl, U. *Phys. Rev. B* **2011**, *84* (15), 153402.

(44) Meyer, J. C.; Geim, A. K.; Katsnelson, M. I.; Novoselov, K. S.; Booth, T. J.; Roth, S. *Nature* **2007**, *446* (7131), 60−63.

(45) Brivio, J.; Alexander, D. T. L.; Kis, A. *Nano Lett.* **2011**, *11* (12), 5148−5153.